ACS OMEGA

Open Access

http://pubs.acs.org/journal/acsodf

Article

Transformation of Fly Ash-Based Oxide Particles into a Functional Silica−Alumina Aerogel and Its Potential Application as an Anti-icing Surface

Esra Bedir, Senem Çitoğlu, and Hatice Duran*

Cite This: *ACS Omega* 2024, 9, 35864−35872

Read Online

ACCESS | Metrics & More | Article Recommendations | Supporting Information

ABSTRACT: Lightweight, surface hydrophobic, highly insulating, and long-lasting aerogels are required for energy conservation and ice-repellent applications. Here, we present the conversion of fly ash to a silica−alumina aerogel (SAA) by utilizing its high silica content. The extracted silica component replaces expensive precursors typically used in conventional aerogel production. Ice adhesion performance was compared to that of polypropylene (PP), an insulating commodity polymer. First, we removed some salt impurities and heavy metals via water and alkaline washing protocols. Then, we produced SAA via the ambient pressure drying method by using trimethylchlorosilane (TMCS) as an adhesion promoter. The newly produced SAA has a surface area of 810 m^2 g^{-1} and shows hydrophobic properties with a contact angle of 140 ± 5°. The thermal conductivity of SAA is 0.0238 W m^{-1} K^{-1} with C_P = 1.1922 MJ m^{-3} K^{-1}. The ice adhesion strength of the PP substrate was calculated as 188.30 ± 51.24 kPa, while the ice adhesion strength of the SAA was measured as 1.21 ± 0.40 kPa, which was about 150 times lower than that of PP. This indicated that SAA had icephobic properties since ice adhesion strength was less than 10 kPa. This study demonstrates that fly ash-based SAA can be utilized as an economical material with a large surface area and exceptional thermal insulation capacity and is free of harmful compounds (heavy metals), making it potentially suitable as an anti-ice thermal insulation material.

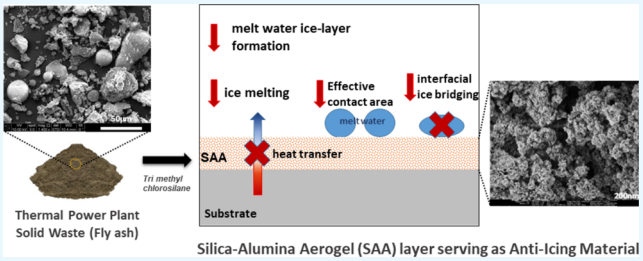

1. INTRODUCTION

Silica-based aerogels have been produced by various precursors such as tetraethoxysilane (TEOS),[1] tetramethoxysilane (TMOS) with mercaptopropyl trimethoxysilane (MPTMS),[2,3] and sodium silicate (Na_2SiO_3).[4] Generally, aerogel production is carried out in two stages. First, a sol−gel process using a mixture of the silane precursor, alcohol, and water is prepared. In the second step, the sol is converted into gel form via hydrolysis and condensation. Finally, the aerogel is obtained after the displacement of the liquid phase drawn from the gel with air. One of the biggest advantages of this method is that it allows the preparation of more homogeneous surfaces at lower temperatures compared to powder technologies. In addition, the reactants used in sol−gel technology are readily available in high purity.

Many methods have been proposed to replace expensive precursors for producing silica aerogels, converting waste into ultralight and ultraporous materials.[5] It is reported that domestic,[6] agricultural,[7] and industrial wastes[8,9] are viable precursors for the production of aerogels due to their widespread availability. Hu et al.[10] used kaolin as a raw material to produce a silica aerogel. By extracting the silica compound in kaolin, they were able to produce an aerogel with a specific surface area of 465.03 m^2 g^{-1} with ambient pressure drying. Alternatively, Tang and Wang[11] produced a silica aerogel by extracting the silica compound contained in rice husk ash by using first the sol−gel method and then applying the supercritical drying method. Their aerogel has a high specific surface area of 597.7 m^2 g^{-1}, and the pore diameter varies between 10 and 60 nm. However, supercritical drying causes some operation risk processing safety issues and is costly due to system maintenance. Therefore, for practical applications, the ambient pressure drying technique is preferred considering the fabrication cost and safety issues. The usage of fly ash (FA) as a precursor material for aerogel fabrication has been gaining momentum in recent years thanks to its composition, including rich SiO_2 and Al_2O_3.[12−16]

Combustion of municipal solid wastes, biomass, and coal in thermal power plants results in the generation of huge amounts of fly ash (FA) residues. FA production is influenced by various factors, such as the type of burning, coal source, and operation conditions. Regardless of their source, these fly ashes have various glassy, spherical silica, and alumina particles

Received: May 21, 2024
Revised: July 26, 2024
Accepted: July 30, 2024
Published: August 7, 2024

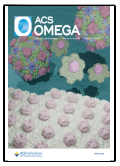

(diameter ranges from 100 nm to 500 μm) that have the potential to be exploited in industry to a large extent.[17,18] However, it should be noted that they contain heavy metal residues even at the parts per million level, which causes concerns about the environment and public health. In recent years, both the elimination of these residues and the effective processing of FAs have become a topic of many investigations. Nevertheless, FA is an attainable raw material for synthesizing aerogels due to its low cost, abundance of natural resources,[8] and sustainability potential.

Silica aerogels have great potential as ice-repellent materials due to their lightweight, low thermal conductivity, and adjustable hydrophobicity.[19] If the solid−air interface is designed correctly, it can be used as a passive ice repellent without any external chemical, heat, or mechanical force. Traditional techniques used to deal with icing problems, such as mechanical defrosting and thermal or chemical processes, are quite costly and less efficient. Another common strategy for removing ice or preventing ice buildup is the use of defrosting fluids (antifreeze). However, this approach must be repeated frequently to be effective, and liquids used for this purpose are known to have a negative impact on the environment.[20] In addition, films that form an aqueous shear layer at the interface are one of the new approaches that have started to be applied in recent years.[21] The importance of the structure of the ice−substrate interface for ice adhesion is obvious. It is well-known that the ice surface is slippery to ice skating blades; that is, it has low adhesion strength due to a premolten surface layer. Due to regelation, pressure or frictional melting, a premolten liquid or liquid-like thin aqueous layer is formed, which is located on the surface of the ice at subzero temperature. The premolten or liquid-like ice sheet can be observed at not only ice−steam but also ice−solid interfaces. Since the thickness of the premolten layer at ice−solid increases with temperature, the use of the premolten layer to effectively reduce ice adhesion has become one of the important strategies for eliminating surface icing. The premolten layer changes the ice−substrate contact from solid−solid to solid−liquid−solid form. This results in disordered and short-range atomistic interactions of van der Waals forces and hydrogen bonds. By rational design of nanostructured solid surfaces to form an interfacial semiliquid layer, ice formation was delayed for 25 h at −21 °C.[20] However, these surfaces have the problem of depletion of the lubricant over time through evaporation or wear of the lubricant with moving drops. Alternatively, solid lubricants have been used at the interfaces of the substrates to facilitate the removal of ice. For example, a layer of alkanes is embedded in the surface of a polymer substrate. Perfluoroalkane wax has been validated as a good lubricant candidate for the production of solid lubricant regenerable surfaces.[21] The perfluoroalkane wax regenerating surface showed low ice adhesion strength (20 kPa) and high mechanical stability. Compared to their liquid counterparts, solid lubricant layers are mechanically more robust in icing/defrosting cycles. However, both liquid and solid lubricating renewable layers are quite limited in their application due to the limited regeneration capacity of the surfaces. The optimal solution to this problem, which is still widely researched today, is focused on the design of passive anti-icing systems that prevent icing or reduce the rate of ice accumulation. This reduces the power consumption required to remove the ice. There are several main strategies for the design of such passive anti-icing formulations. One of them is based on the lowering of the ice adhesion strength.[22] The following approaches are commonly used to prevent icing by making chemical or physical changes to the surface: pushing water droplets coming to the surface (chemical/physical hydrophobic surface design), delaying ice nucleation (chemical), suppressing ice growth (chemical), and weakening ice adhesion (physical/chemical). In fact, biomimetic models have been the inspiration for these approaches. For example, superhydrophobic surfaces inspired by the lotus leaf produced to repel water droplets delay ice nucleation.[23] Similarly, omniphobic carnivorous pitcher plant-inspired slippery liquid-infused porous surfaces have been developed as multiple anti-icing materials.[24,25] It is generally believed that superhydrophobic surfaces exhibit anti-icing properties. However, new reports have cast doubt on the effectiveness of this approach, and such surfaces are not necessarily the best solution. For example, frost formation at high humidity and water condensation in the rough surface of superhydrophobic materials have caused locally high ice adhesion strength due to the large solid−ice contact area.[26] Furthermore, Kulinich et al.[27] observed that repeated icing/defrosting cycles on superhydrophobic surfaces result in increased ice adhesion strength over time due to the erosion of the micro/nanostructure of the superhydrophobic surface. The main approach of anti-icing surfaces reported in the literature recognizes only the ice−substrate interface and its adjacent regions being of a static nature. However, depending on the purpose and location of use, the general properties of ice−substrate interfaces vary with time, temperature, and various external stimuli. The heat transfer retardant effect of the highly porous aerogel further supported the potential of using a layer of low thermal conductivity to avoid icing problems. For instance, Zhao et al. successfully overcame ice melting and its subsequent refreezing by combining the synergies between thermal insulation and superhydrophobicity on solid surfaces.[19] A thermally insulative layer restricts solid-to-ice heat transfer, reducing ice melting and thus causing meltwater ice layer formation, whereas a hydrophobic layer lowers the effective contact area of any meltwater present on the surface, minimizing interfacial ice bridging. This collective effect may further reduce the snow adhesion strength. Li et al.[28] developed micro- and mesoporous halloysite aerogels with low icing temperatures to form the anti-icing coating. Very recently, Xiong et al.[29] introduced an aerogel-incorporated foam architecture, improving anti-icing performance and durability. Technically, to prevent the icing of a surface, the following conditions are required: (i) a low ice adhesion strength of 0.2−10 kPa (usually, icephobic surfaces are defined as having an ice adhesion strength of μ < 100 kPa and require a much lower strength of μ < 10 kPa for the passive removal of ice)[30] and (ii) an easy-to-apply, large-scale deicing method.

In this study, we developed a hydrophobic and thermally insulating silica−alumina aerogel (SAA) that prevents ice adhesion and does not require any external mechanical, magnetic, or electrical energy to remove ice. We used lignite-based fly ash (LBFA) for SAA synthesis, since it has pozzolanic properties and fine particles. First, the silica content of the LBFA was increased by water washing and alkaline treatment. This treatment also removed some impurities, such as salts and heavy metals, and increased the specific surface area of pristine LBFA. Then, a light silica−alumina aerogel (SAA) enriched with silica was formed by an ambient pressure drying method. The newly produced SAA is hydrophobic and has a very large specific surface area. The thermal conductivity and heat

https://doi.org/10.1021/acsomega.4c04802
ACS Omega 2024, 9, 35864−35872

capacity of SAA were measured, and its use as an icephobic material was compared with polypropylene (PP), a commercial refrigerator ice mold material.

2. EXPERIMENTAL SECTION

2.1. Materials and Methods. *2.1.1. Materials.* Lignite-based fly ash (LBFA) was taken from a Turkish-origin Thermal Power Plant. The chemical content of LBFA is given in Table 1. Trimethylchlorosilane (TMCS, 98%), hexane (95%), sodium hydroxide (NaOH, 99%), sodium bicarbonate ($NaHCO_3$), hydrochloric acid (HCl, 37%), ammonium hydroxide (NH_4OH, 25%), and ethyl alcohol (EtOH, 99.9%) were purchased from Sigma-Aldrich.

Table 1. Chemical Content of Pristine, Washed, and Alkaline-Treated LBFA

oxide compounds (excluding oxide compounds below 1%)	pristine LBFA (%)	washed LBFA (%)	alkaline-treated LBFA (%)
SiO_2	53.193	53.571	58.301
Al_2O_3	28.377	27.860	27.612
Fe_2O_3	7.018	6.400	6.161
K_2O	4.500	5.347	5.113
MgO	2.068	1.925	1.057
CaO	1.818	1.914	1.885
TiO_2	1.232	1.412	1.331

2.1.2. LBFA Washing. LBFA (100 g) was diluted with distilled water (500 mL) to remove impurities (such as organic sodium salts) from the pristine fly ash. The mixture was stirred at 350−400 rpm for 4 h at 50 °C with a magnetic stirrer. Then, the solution was filtered through a filter paper. This process was repeated at least three times until obtaining a clear supernatant. Finally, the solid part was dried in a vacuum oven at 120 °C for 2−3 h.

2.1.3. Alkaline Treatment of LBFA. An alkaline solution ($NaOH/NaHCO_3$, pH = 10.5) was prepared for silica enrichment and heavy metal removal. Then, LBFA was added in solution (5:1) and held in the solution for 5 min at 60 °C. Finally, LBFA was removed from the solution and washed with distilled water. Subsequently, LBFA was dried in a muffle furnace at 350 °C for 1 h.

2.2. Silica−Alumina Aerogel (SAA) Preparation. The LBFA powder was added to a 3 M HCl solution and stirred at 400 rpm for 5−10 min (Figure S1a). After vacuum filtration, a gel was obtained at around pH = 3 with the aid of NH_4OH (25%; Figure S1b). The mixture was left at 80 °C for 2 h to further set the gelation. Then, the gel was cooled to 50 °C and kept at this temperature for 3−4 h to form a three-dimensional (3D) network structure. Once the gel structure was formed, it was kept in absolute ethanol at 50 °C for 24 h for solvent exchange. A mixture of trimethylchlorosilane and ethanol (TMCS/ethanol, 8:2 v/v) was prepared (Figure S1c). Then, the mixture was added to the gel, and the mixture was kept at room temperature for 24 h. The gel was filtered by washing it with hexane (Figure S1d). After filtering, it was kept in a fume hood for a while to remove excess solvent. Then, it was kept in a vacuum oven at 100 °C for 2 h and then at 200 °C for 2 h for further drying. Finally, a white, granular SAA was obtained (Figure S1e).

2.3. Characterization. The chemical content of LBFA was analyzed by an X-ray fluorescence (XRF) (Rigaku ZSX Primus II) instrument. Surface chemical and high-resolution elemental analyses were used to follow the chemical modifications on the silica aerogel surface. X-ray photoelectron spectroscopy (XPS, Thermo Scientific K-Alpha) with an Al Kα (1486.6 eV) monochromatic beam was used for this analysis. Scanning electron microscopy (SEM) was performed to view the morphologies of pristine LBFA and silica aerogel. This analysis was performed with a Quanta 400 FEG scanning electron microscope. SEM images and energy dispersive X-ray (EDX) analysis of fly ash were obtained using a Zeiss Evo 50 scanning electron microscope equipped with an Oxford EDX detector. Transmission electron microscopy (TEM) was performed to visualize the formed 3D network and the architecture of the pores. This analysis was performed using an FEI Tecnai G2 F20 instrument using an accelerator voltage of 200 kV. Brunauer−Emmett−Teller (BET) analysis (Nova 1000e) was used to determine the silica aerogel's surface area and pore size via N_2 adsorption−desorption isotherms (T = 77 K). The specific surface area was measured based on the amount of N_2 gas adsorbed at various partial pressures (five points $0.1 < P/P_0 < 0.2$). A Malvern Panalytical X'Pert Pro Multi-Purpose Diffractometer X-ray diffraction (XRD) was used to determine the phase and chemical composition of the silica aerogel material. The X-ray source is a ceramic X-ray tube with a Cu Kα anode (λ = 1.540 Å). The X-ray tube was operated at 45 kV and 40 mA. Water contact angle (WCA) measurements on SAA and PP films were performed by an Attension by KSV Instruments. The "sessile drop" method was used for this measurement from each location (corners and midpoint) at a minimum of three points of each film. Thermogravimetric analysis (TGA, Q500 V20.13 Build 39) was used to characterize the thermal stability of the aerogel and also to calculate the amount of organic content. The analysis was carried out in a nitrogen environment, starting from room temperature and heating up to 900 °C with a rate of 10 °C min^{-1}.

2.3.1. Thermal Conductivity Measurements. The thermal conductivity values of SAA (20 mm × 20 mm × 1 mm) ($L \times W \times H$) and PP (25 mm × 25 mm × 2.5 mm) were obtained by the Hot Disk (TPS 2500S) method in double-side mode. A Kapton insulated disc-type sensor with a radius of 2.001 mm (sensor 7577), which acts as both a heater (current provider) and a temperature sensor (resistance thermometer), was placed between two substrates, with each surface facing the sensor. The instrument was capable of measuring with step sensitivity in the range of 0.005−1800 W m^{-1} K^{-1} (±3%). The PP and SAA substrates were placed between two foam insulators for thermal insulation. In thermal conductivity measurements, the output power (3−10 mW) and measurement time were selected to meet some requirements (probing depth sample thickness, 0.33 < total characterization time < 1, maximum temperature increase: 2−5 K). The specific heat capacity (C_P) and thermal conductivity constant (k) were calculated using the Hot Disk device interface program (Thermal Analyzer) using a time-dependent graph of the temperature change during measurement. All measurements were carried out at 26 ± 2 °C, waiting at least 10 min to reach thermal equilibrium between each measurement.

2.3.2. Ice Adhesion Test. A commercial polypropylene (PP) ice mold (obtained from Arçelik A.Ş. Refrigerator Plant, Eskişehir-Türkiye) was taken as a reference to better evaluate the potential for SAA to be used as an anti-icing material. PP has a number-average molecular weight M_n of 320 kg mol^{-1}, a

https://doi.org/10.1021/acsomega.4c04802
ACS Omega 2024, 9, 35864−35872

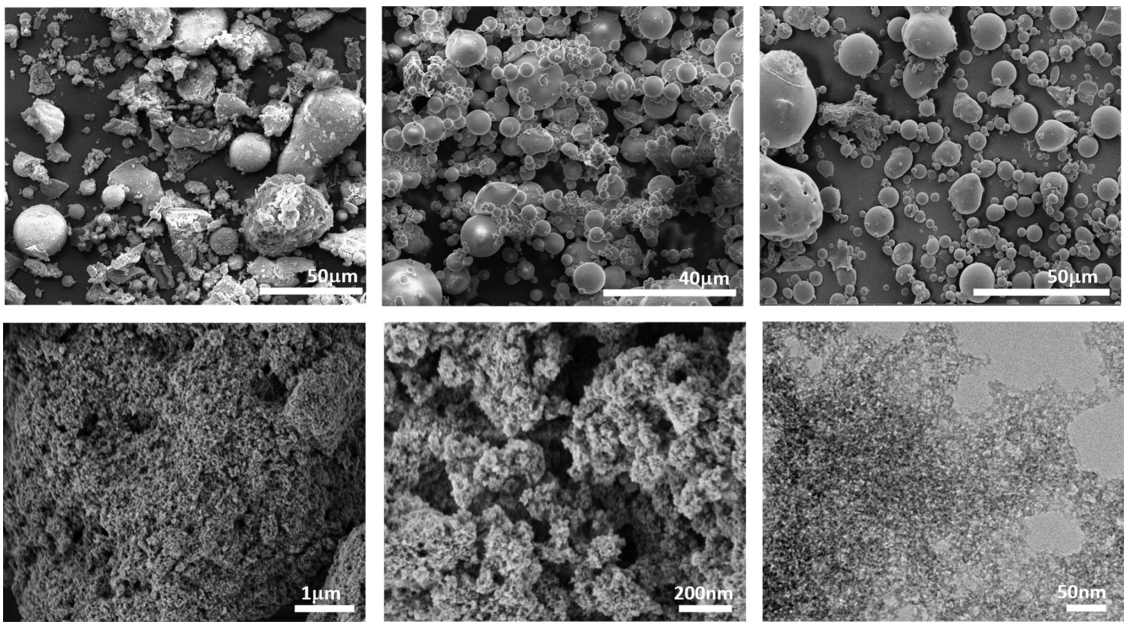

Figure 1. SEM image of (a) pristine LBFA, (b) washed LBFA, (c) alkaline-activated LBFA, and (d, e) SAA at various magnifications. (f) TEM image of the SAA.

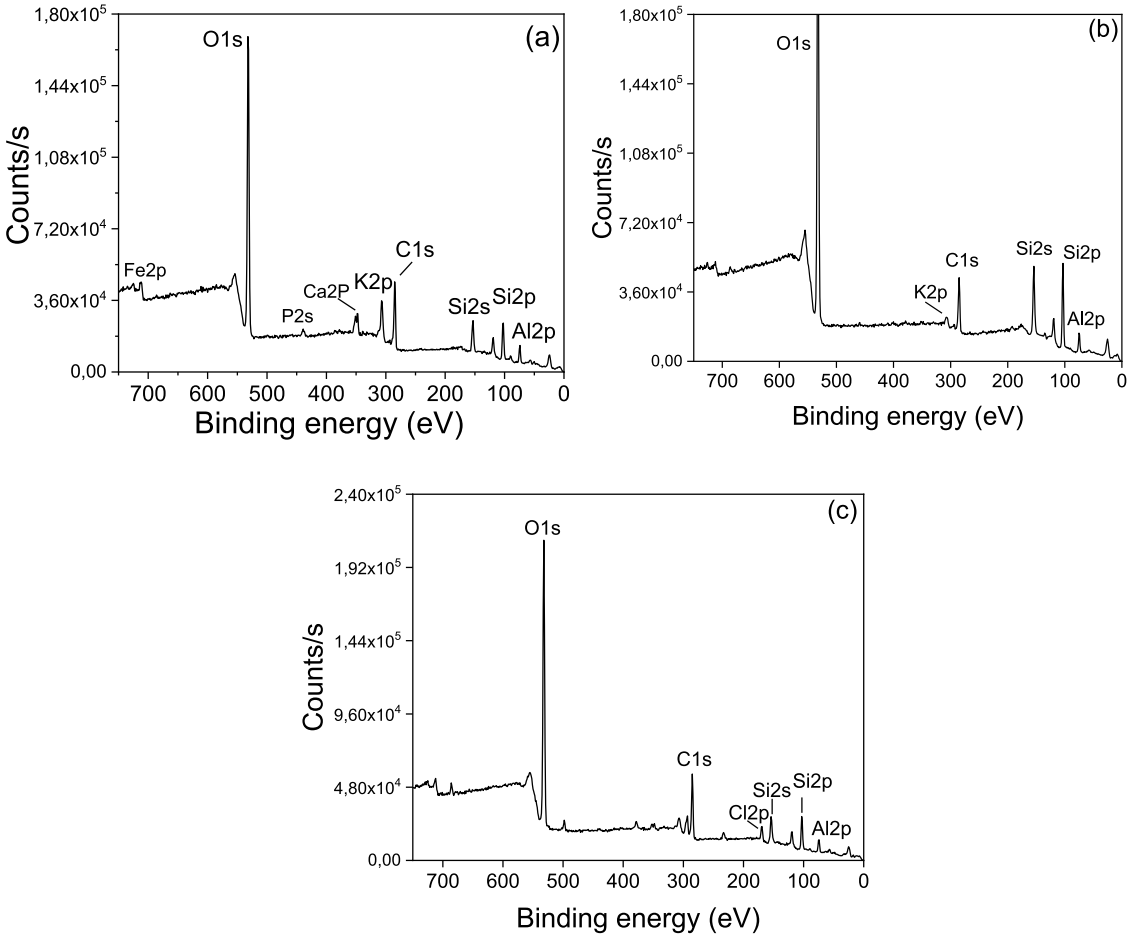

Figure 2. X-ray photoelectron spectroscopy scans of (a) pristine LBFA, (b) alkaline-activated LBFA, and (c) SAA.

crystallinity of 57.2%, and a thermal decomposition temperature of 456 °C.

The adhesion strength of ice on substrates was measured by a slip/peel tester (IMASS SP-2100) equipped with a force sensor. The experimental setup is shown in Figure S2. A 1.5 cm long part cut from the wide end of a 200 μL polypropylene pipet tip (ISOLAB, transparent) was used as an ice mold. The ice mold (inner diameter of 0.5 cm and height of 1.5 cm)

https://doi.org/10.1021/acsomega.4c04802
ACS Omega 2024, 9, 35864−35872

placed on the sample surface in the refrigerator was filled with 200 μL of Milli-Q water and allowed to freeze at −18 °C for 24 h. The selected freezing temperature (−18 °C) and time (24 h) were determined according to typical household refrigerator conditions. The force transducer arm was placed around the ice mold, and the force−time graph was recorded while the sample was moved very slowly at a constant speed of 0.3 mm s^{-1}. The ice adhesion force (kN) measured by the device was normalized according to the contact area (m^2), and the ice adhesion strength was calculated in kilopascals (kPa). Maximum force values were used in the ice adhesion strength calculations. Each test was performed at least three times.

3. RESULTS AND DISCUSSION

The chemical compositions of the pristine, washed, and alkali-treated LBFA samples were analyzed by XRF as oxide compounds, as listed in Tables 1 and S1. Water washing is used to remove impurities from pristine LBFA. The results show that washing is effective for the removal rate of Na, Cr, Ni, Cu, Ga, Ba, Pb, and S ions. The water washing procedure can also remove heavy metal ions such as Cu, Pb, and Cr (Table S1). Alkaline-treated LCFA has slightly higher SiO_2 compared to that of pristine LBFA (Table 1). As the temperature is raised to 50 °C, OH^- anions react selectively with Al_2O_3 with a higher etching rate compared to silica and other oxides.[31]

After the elimination of impurities and increasing the silica content, LBFA was subjected to the aerogel formation process. The gelation begins at around a pH value of 3. The gel was left at 80 °C for 2 h to further increase the concentration. When a 3D network structure was obtained, it was kept in absolute ethanol at 50 °C for 24 h for solvent exchange. The mixture was kept in hexane/TMCS/ethanol at room temperature for 24 h. Afterward, the gel was filtered and washed with hexane. Consequently, a white gel structure was formed. Finally, after drying in a vacuum oven at 100 °C for 2 h/at 200 °C for 2 h, the SAA was obtained. The morphologies of LBFAs and the SAA were examined by SEM and TEM (Figure 1). The pristine LBFA has micro- and nanoparticles with wide size distribution. The particle diameter ranged from 500 nm to 14 μm, and the mean diameter was calculated as 2.23 ± 2.17 μm. The needle-like substances and dense inclusions of salts on the particle surface can be clearly distinguished from the image (Figure 1a). On the other hand, washing and base treatment steps (Figure 1b,c) preserved the spherical form of the particles and resulted in the removal of water-soluble salts. The rough surface structure of the aerogel containing many pores and nanoparticles is also visible in Figure 1d,e. A large number of pores are visualized as a 3D network structure and the continuous connection between the particles.

Surface elemental compositions were analyzed by XPS. The survey scan of pristine LBFA, alkaline-activated LBFA, and SAA is shown in Figure 2. The signals at 152.4 and 102.23 eV belong to the binding energies of Si 2s and Si 2p orbitals of Si. These two signals are present for all samples. Similarly, C 1s and O 1s orbital signals are also present at 284.89 and 531.91 eV, respectively. The source of the C 1s signal can be attributed to the unburnt carbon and adsorbed CO_2. Al 2p signal appearing at 74.6 eV arises from the Al oxide component, while the signal at 711.8 eV belongs to Fe_2O_3. After the alkaline treatment step, the signals of Ca and P elements present in pristine LBFA disappeared, while K peak intensity decreased significantly (Figure 2b). In addition, the C/O ratio decreased from 0.32 to 0.11 for pristine LBFA and alkaline-treated LBFA, respectively. The appearance of the Cl 2p orbital signal at 198 eV belonging to Cl−Si validated the functionalization of aerogel TMCS. Furthermore, the signal at 103.1 eV binding energy corresponds to the Si−C−(−H) bond, while 285.1 eV binding energy corresponds to the C−O(−H) bond. Also, the binding energy corresponding to the C−O(−Si) bond was not observed for the SAA modified with TMCS. This might be due to the hydrolysis of −OR groups to form −Si−OH groups (Figure 2c). XPS scans confirm that the silica skeleton, which has a −Si−OH group both on its surface and inside, is successfully silanated and forms a Si−CH_3 group. The process of silanization of the SAA with TMCS is given in reactions 1 and 2.

$$(CH_3)_3Si{-}Cl + \equiv Si{-}OH \rightarrow \equiv Si{-}O{-}Si(CH_3)_3 + HCl \quad (1)$$

$$(CH_3)_3Si{-}OC_2H_5 + \equiv Si{-}OH \rightarrow \equiv Si{-}O{-}Si(CH_3)_3 + CH_3CH_2OH \quad (2)$$

The crystal structure of the aerogel was investigated by XRD analysis (Figure 3). There is a wide semiotic peak centered at

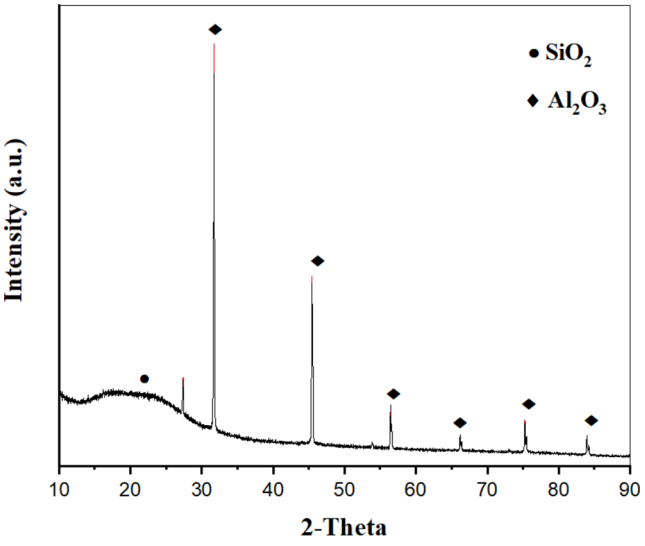

Figure 3. XRD analysis of the SAA.

around 2θ = 26° and appears to the left in a sprawling and asymmetrical appearance. This corresponds to the typical pattern of the amorphous silica (SiO_2) compound. The sharp peaks at high order on the diffractograms were compared to XRD standards for α- and γ-Al_2O_3 JCPDS references (file nos. 00-005-0712, 00-010-0425, and 004-0787) in the International Centre for Diffraction Data (ICDD) database. The crystallographic angles/planes at 2θ = 32.9° (220), 45.8° (400), and 67.2° (440) are the characteristic peaks of the γ-Al_2O_3 phase with a cubic structure, while the crystallographic angle/plane at 2θ = 57.5° (116) is the characteristic peak of the α-Al_2O_3 phase.

The BET analysis was performed to measure the surface area, pore size, and pore size distribution of the aerogel. The degassing was performed at 200 °C for 2 h, and then N_2 adsorption−desorption analysis was conducted. The specific surface area was calculated from five points according to the multipoint BET method, with a maximum P/P_0 = 0.2. The

https://doi.org/10.1021/acsomega.4c04802
ACS Omega 2024, 9, 35864−35872

total surface area of pristine LBFA is approximately 174 m^2 g^{-1}. However, it is desirable to have a specific surface area of more than 200 m^2 g^{-1} for an ideal thermal insulation material. The specific surface area of the SAA, on the other side, is approximately 810 m^2 g^{-1}. This value is in line with the literature since the specific surface area of a typical silica aerogel varies between 550 and 950 m^2 g^{-1}.[32,33] The N_2 adsorption−desorption isotherm (Figure S3a) complies with type V in the physisorption isotherm classification according to the International Union of Pure and Applied Chemistry (IUPAC).[34] This indicates that the synthesized SAA is composed of micropores. The adsorption hysteresis loop fits with the type H3 behavior, indicating plate-like particles in the SAA. The pore size distribution was calculated according to density functional theory (DFT). The pore radius is concentrated at 10−30 Å, with an average radius of 17.3 Å (Figure S3b).

Thermogravimetric analysis was performed to examine the thermal stability of the obtained SAA (Figure 4). There was an

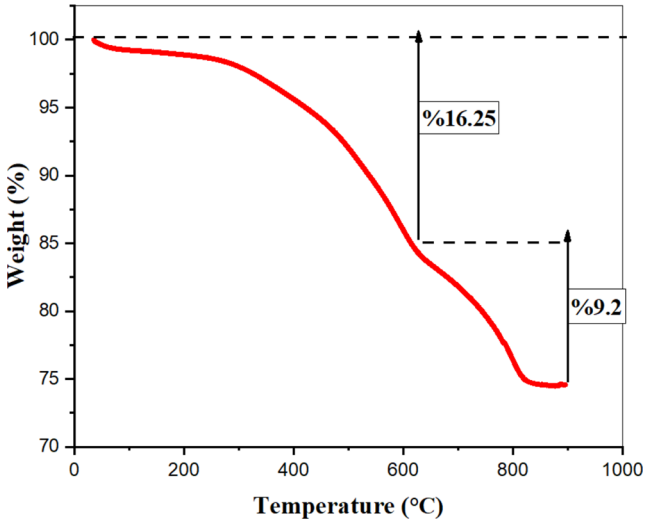

Figure 4. TGA curve of the SAA.

approximately 16.25% mass loss between 0 and 590 °C, referring to the removal of a small amount of physically absorbed water trapped in the material, as well as the oxidation of methyl groups ($-CH_3$) on the surface of the aerogel.[35,36] The mass loss continues with increasing temperature. The mass loss between 591 and 798 °C may result from the decomposition of the SA backbone due to thermal degradation.

The wettability of SAA and PP was performed by measuring the surface water contact angles (WCAs). The WCA of the PP film was found to be 89.2 ± 2.0° (Figure 5a), while SAA showed a higher WCA of 140 ± 5°. The larger standard deviation of SAA samples arises from the surface roughness of the film. Even though PP and SAA have different chemical structures, both contain $-CH_3$ groups that exhibit a hydrophobic behavior. SAA's superior hydrophobicity, with a higher water contact angle compared to PP, may be attributed to its uniform distribution of low surface energy silane molecules combined with a rough surface.[37] In contrast, the crystallinity of the PP chains leads to more van der Waals interchain interactions. The nonpolar $-CH_3$ pendant groups on the densely packed PP film make them more accessible to SAA. Moreover, the aerogel's molecular structure with low surface energy and its nano/microrough surface reduce liquid−solid contact,[38] resulting in Cassie−Baxter wetting behavior.[39,40] These physical and chemical effects collectively prevent water droplets from seeping into the aerogel, enhancing its superhydrophobic nature.

The heat conduction capacities of SAA and PP were also measured at 26 ± 2 °C, with an output power of 4−10 mW (measuring time of 1−5 s). The thermal conductivity constant of PP was measured as 0.2224 ± 0.0017 W m^{-1} K^{-1} (C_P = 1.1065 ± 0.0427 MJ m^{-3} K^{-1}). This value is actually consistent with the thermal conductivity of typical bulk polymers, which range between 0.1 and 0.5 W m^{-1} K^{-1}.[41,42] On the other hand, the thermal conductivity of SAA is 0.0238 W m^{-1} K^{-1} with C_P = 1.1922 MJ m^{-3} K^{-1}. PP has 1 order of magnitude higher thermal conductivity than SAA. It is also known that thermal insulation is correlated to the material's porosity. According to ISO and EN Standards,[43] in order to call a material a thermal insulator, it must meet the condition of k < 0.065 W m^{-1} K^{-1}. The resulting SAA clearly meets the condition of the thermal insulation material.

The ice adhesion strength of the PP substrate was calculated as 188.30 ± 51.24 kPa (Figure 6a), while the ice adhesion strength of the SAA was much lower (1.21 ± 0.40 kPa; Figure 6b), which was about 150 times lower than that of PP. It is also apparent that the ice on the SAA substrate started to break in the early stages of adhesion testing. While the ice on the PP substrate resisted breaking for approximately 15 s. This shows that the adhesion between PP and ice is much stronger. We attempted to relate the low ice adhesion strength of SAA to its thermal conductivity and surface wettability, although this is quite complicated. This is because the other surface characteristics such as roughness and hardness as well as the nucleation mechanism (homogeneous or heterogeneous) can affect the friction regime. Indeed, Ozbay[44] showed that ice adhesion

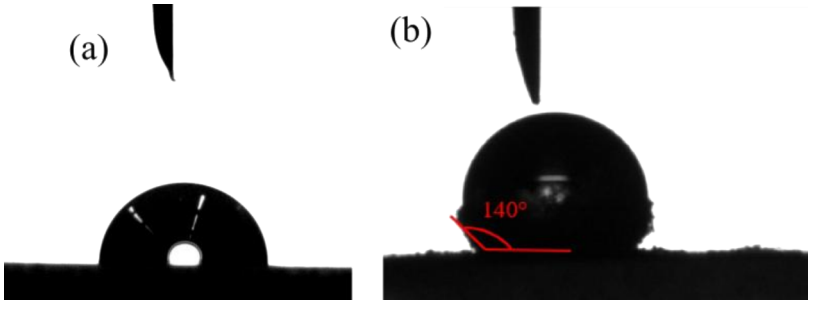

Figure 5. Images depicting WCAs of (a) PP and (b) the SAA.

https://doi.org/10.1021/acsomega.4c04802
ACS Omega 2024, 9, 35864−35872

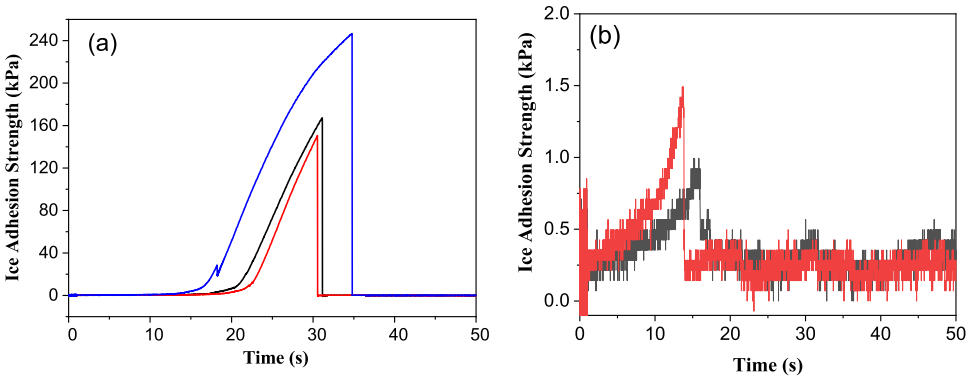

Figure 6. Ice adhesion strength−time graphs of (a) PP and (b) SAA samples measured under a constant pulling speed (0.3 mm s^{-1}). Different colors show repeated measurement results.

strength decreased and drop freezing time increased as the surface hydrophobicity increased. They related this dependency on delayed ice nucleation due to its low surface free energy. However, many researchers have recently clearly proved that surface hydrophobicity alone is not sufficient for low ice adhesion.[45,46] Certainly, the thermal conductivity of the substrates in contact with the droplet should be taken into account. The effect of thermal conductivity on ice friction was studied for various materials with different thermal conductivities at a wide range of temperatures and sliding velocities.[47] For instance, when using titanium alloy, whose thermal conductivity is 4 times lower than aluminum, the ice friction coefficient of titanium alloy was found to be 65−85% lower than that of aluminum at very low sliding velocities (<0.4 mm s^{-1}). Our results are in line with respect to the thermal conductivity versus ice adhesion strength trend described by Kietzig[47] and others.[48,49] The higher thermal conductivity of the PP substrate causes more heat to be transmitted to the environment so that less heat is available at the interface to form meltwater, which contributes to lubrication. In other words, the heat is trapped at the interface due to the limited thermal conductivity of the insulating SAA that lowers the coefficient of friction at the boundary, where interlocking asperite contacts contribute to friction resistance.

The effect of the thermal conductivity of the substrate on the ice adhesion strength might also be related to the nature (structure) of the ice layer formed at the interface as a result of the surface water interaction during the icing process. For example, some studies[44,47,49] showed that freezing at the insulated surface water interface started later than in the conductive material. This means that some amount of water is confined between ice and the insulating surface. Chen et al.[49] clearly demonstrated that the structure and thickness of the ice layer formed at the interface change depending on the thermal conductivity of the substrate. It is likely that even a layer of water that can act as a lubricant is trapped between these two layers without freezing. Since this interface boundary layer is very thin, it needs to be investigated in detail with advanced research techniques. In a previous study,[50] we found that nanoconfined water crystallized differently compared to bulk water, as it showed a transition from heterogeneous nucleation of hexagonal ice to homogeneous nucleation of predominantly cubic ice form.

4. CONCLUSIONS

The ability to change the surface properties of a material as necessary can expand and diversify its application areas. In this study, a low-cost silica−alumina aerogel (SAA) was produced from lignite-based fly ash (LBFA), which is a byproduct of thermal power plants, via the ambient pressure drying method. SAA is free from heavy metals by alkali treatment for large-scale aerogel production and a wider range of applications. The specific surface area of the SAA is approximately 810 m^2 g^{-1}, and the thermal conductivity is around 0.0238 W m^{-1} K^{-1} with C_p = 1.1922 MJ m^{-3} K^{-1}. Additionally, SAA possesses hydrophobic properties with a WCA of 140 ± 5°. We also measured the ice adhesion strength of SAA as 1.21 ± 0.40 kPa, which clearly indicated that SAA had icephobic properties since the ice adhesion strength was less than 10 kPa. With such a high surface area, hydrophobic surface property, and low thermal conductivity, SAA has the potential to be used in refrigerators as both an insulating and anti-ice material.

There is an interplay among the icephobicity, thermal conductivity, and wettability of the substrate. We think that the nucleation mechanism of the liquid (metastable) at the substrate−ice interface, which is entrapped due to poor heat transfer, also contributes to ice adhesion strength. However, this issue requires more basic research and will be the subject of our next study.

■ ASSOCIATED CONTENT

Supporting Information

The Supporting Information is available free of charge at https://pubs.acs.org/doi/10.1021/acsomega.4c04802.

Test setup used for measuring ice adhesion strength; N_2 adsorption−desorption and pore radius curves of SAA; and XRF elemental composition of LBFA before and after wet treatments (PDF)

■ AUTHOR INFORMATION

Corresponding Author

Hatice Duran − *Department of Materials Science & Nanotechnology Engineering, TOBB University of Economics and Technology, 06560 Ankara, Türkiye; UNAM—National Nanotechnology Research Center and Institute of Materials Science and Nanotechnology, Bilkent University, 06800 Ankara, Türkiye;* orcid.org/0000-0001-6203-3906; Email: hduran@etu.edu.tr

https://doi.org/10.1021/acsomega.4c04802
ACS Omega 2024, 9, 35864−35872

Authors

Esra Bedir − *Department of Materials Science & Nanotechnology Engineering, TOBB University of Economics and Technology, 06560 Ankara, Türkiye*

Senem Çitoğlu − *Department of Materials Science & Nanotechnology Engineering, TOBB University of Economics and Technology, 06560 Ankara, Türkiye*

Complete contact information is available at: https://pubs.acs.org/10.1021/acsomega.4c04802

Author Contributions

E.B.: investigation, visualization, and methodology. S.Ç.: investigation, visualization, and editing. H.D.: conceptualization, writing—review and editing, project administration, supervision, validation, visualization, and writing—original draft.

Notes

The authors declare no competing financial interest.

■ ACKNOWLEDGMENTS

H.D. and S.Ç. gratefully acknowledge TÜBİTAK TEYDEB for the financial support of project 5220156 and COST Action CA20126 "Network on Porous Semiconductors and Oxides" supported by COST (European Cooperation in Science and Technology).

■ REFERENCES

(1) Venkateswara Rao, A.; Bhagat, S. D. Synthesis and Physical Properties of TEOS-Based Silica Aerogels Prepared by Two Step (Acid−Base) Sol−Gel Process. *Solid State Sci.* **2004**, *6* (9), 945−952.

(2) Štandeker, S.; Veronovski, A.; Novak, Z.; Knez, Ž. Silica Aerogels Modified with Mercapto Functional Groups Used for Cu(II) and Hg(II) Removal from Aqueous Solutions. *Desalination* **2011**, *269* (1), 223−230.

(3) Venkateswara Rao, A.; Bhagat, S. D.; Hirashima, H.; Pajonk, G. M. Synthesis of Flexible Silica Aerogels Using Methyltrimethoxysilane (MTMS) Precursor. *J. Colloid Interface Sci.* **2006**, *300* (1), 279−285.

(4) Falsafi, M. H.; Moghaddas, M.; Moghaddas, J. Removal of Heavy Metals from Synthetic Wastewater Using Silica Aerogel- Activated Carbon Composite by Adsorption Method. *J. Appl. Res. Water Wastewater* **2020**, *7* (1), 90−96.

(5) Nguyen, P. T. T.; Do, N. H. N.; Goh, X. Y.; Goh, C. J.; Ong, R. H.; Le, P. K.; Phan-Thien, N.; Duong, H. M. Recent Progresses in Eco-Friendly Fabrication and Applications of Sustainable Aerogels from Various Waste Materials. *Waste Biomass Valorization* **2022**, *13* (4), 1825−1847.

(6) Lee, K.; Shabnam, L.; Faisal, S. N.; Hoang, V. C.; Gomes, V. G. Aerogel from Fruit Biowaste Produces Ultracapacitors with High Energy Density and Stability. *J. Energy Storage* **2020**, *27*, No. 101152.

(7) Permatasari, N.; Sucahya, T. N.; Dani Nandiyanto, A. B. Review: Agricultural Wastes as a Source of Silica Material. *Indones. J. Sci. Technol.* **2016**, *1* (1), 82−106.

(8) Do, N. H. N.; Tran, H.; Doan, H.; Pham, N.; Le, K.; Le, P. Advanced Fabrication of Lightweight Aerogels from Fly Ash for Thermal Insulation. *VNUHCM J. Eng. Technol.* **2021**, *4* (1), 637−644.

(9) Asim, N.; Badiei, M.; Alghoul, M. A.; Mohammad, M.; Fudholi, A.; Akhtaruzzaman, M.; Amin, N.; Sopian, K. Biomass and Industrial Wastes as Resource Materials for Aerogel Preparation: Opportunities, Challenges, and Research Directions. *Ind. Eng. Chem. Res.* **2019**, *58* (38), 17621−17645.

(10) Hu, W.; Li, M.; Chen, W.; Zhang, N.; Li, B.; Wang, M.; Zhao, Z. Preparation of Hydrophobic Silica Aerogel with Kaolin Dried at Ambient Pressure. *Colloids Surf., A* **2016**, *501*, 83−91.

(11) Tang, Q.; Wang, T. Preparation of Silica Aerogel from Rice Hull Ash by Supercritical Carbon Dioxide Drying. *J. Supercrit. Fluids* **2005**, *35* (1), 91−94.

(12) Shen, M.; Jiang, X.; Zhang, M.; Guo, M. Synthesis of SiO2−Al2O3 Composite Aerogel from Fly Ash: A Low-Cost and Facile Approach. *J. Sol-Gel Sci. Technol.* **2020**, *93* (2), 281−290.

(13) Zhu, J.; Guo, S.; Li, X. Facile Preparation of a SiO2−Al2O3 Aerogel Using Coal Gangue as a Raw Material via an Ambient Pressure Drying Method and Its Application in Organic Solvent Adsorption. *RSC Adv.* **2015**, *5* (125), 103656−103661.

(14) Wu, X.; Fan, M.; Mclaughlin, J. F.; Shen, X.; Tan, G. A Novel Low-Cost Method of Silica Aerogel Fabrication Using Fly Ash and Trona Ore with Ambient Pressure Drying Technique. *Powder Technol.* **2018**, *323*, 310−322.

(15) Cheng, Y.; Xia, M.; Luo, F.; Li, N.; Guo, C.; Wei, C. Effect of Surface Modification on Physical Properties of Silica Aerogels Derived from Fly Ash Acid Sludge. *Colloids Surf., A* **2016**, *490*, 200−206.

(16) Shi, F.; Liu, J.-X.; Song, K.; Wang, Z.-Y. Cost-Effective Synthesis of Silica Aerogels from Fly Ash via Ambient Pressure Drying. *J. Non-Cryst. Solids* **2010**, *356* (43), 2241−2246.

(17) Kozbek, A. Y.; Şahin, K.; Sarı, E.; Bedir, E.; Yüce, F. G.; Çitoğlu, S.; Duran, H. Evaluation of Amine Functionalized Thermal Power Plant Solid Waste for Industrial Wastewater Remediation. *Adsorpt. Sci. Technol.* **2022**, *2022*, No. 8335566.

(18) Dogar, S.; Nayab, S.; Farooq, M. Q.; Said, A.; Kamran, R.; Duran, H.; Yameen, B. Utilization of Biomass Fly Ash for Improving Quality of Organic Dye-Contaminated Water. *ACS Omega* **2020**, *5* (26), 15850−15864.

(19) Zhao, X.; Zarasvand, K. A.; Pope, C.; Golovin, K. Thermal Insulation and Superhydrophobicity Synergies for Passive Snow Repellency. *ACS Appl. Mater. Interfaces* **2022**, *14* (18), 21657−21667.

(20) Chernyy, S.; Järn, M.; Shimizu, K.; Swerin, A.; Pedersen, S. U.; Daasbjerg, K.; Makkonen, L.; Claesson, P.; Iruthayaraj, J. Superhydrophilic Polyelectrolyte Brush Layers with Imparted Anti-Icing Properties: Effect of Counter Ions. *ACS Appl. Mater. Interfaces* **2014**, *6* (9), 6487−6496.

(21) Sandhu, A.; Walker, O. J.; Nistal, A.; Choy, K. L.; Clancy, A. J. Perfluoroalkane Wax Infused Gels for Effective, Regenerating, Anti-Icing Surfaces. *Chem. Commun.* **2019**, *55* (22), 3215−3218.

(22) Antonini, C.; Innocenti, M.; Horn, T.; Marengo, M.; Amirfazli, A. Understanding the Effect of Superhydrophobic Coatings on Energy Reduction in Anti-Icing Systems. *Cold Reg. Sci. Technol.* **2011**, *67* (1), 58−67.

(23) Lin, Y.; Chen, H.; Wang, G.; Liu, A. Recent Progress in Preparation and Anti-Icing Applications of Superhydrophobic Coatings. *Coatings* **2018**, *8* (6), 208.

(24) Wooh, S.; Vollmer, D. Silicone Brushes: Omniphobic Surfaces with Low Sliding Angles. *Angew. Chem., Int. Ed.* **2016**, *55* (24), 6822−6824.

(25) Baumli, P.; D'Acunzi, M.; Hegner, K. I.; Naga, A.; Wong, W. S. Y.; Butt, H.-J.; Vollmer, D. The Challenge of Lubricant-Replenishment on Lubricant-Impregnated Surfaces. *Adv. Colloid Interface Sci.* **2021**, *287*, No. 102329.

(26) Varanasi, K. K.; Deng, T.; Smith, J. D.; Hsu, M.; Bhate, N. Frost Formation and Ice Adhesion on Superhydrophobic Surfaces. *Appl. Phys. Lett.* **2010**, *97* (23), No. 234102.

(27) Kulinich, S. A.; Farhadi, S.; Nose, K.; Du, X. W. Superhydrophobic Surfaces: Are They Really Ice-Repellent? *Langmuir* **2011**, *27* (1), 25−29.

(28) Li, H.; Li, Q.; Liu, H.; Cao, K.; Zhang, P.; Liu, T.; Wang, D.; Liao, X.; Wei, D. Fabrication of Anti-Icing Surface with Halloysite Spherical Microcapsule. *J. Mater. Res.* **2020**, *35* (21), 2887−2896.

(29) Xiong, Y.; Zhang, Z.; Liu, Y.; Ye, M.; Hu, C.; Chen, J.; Yan, H.; Huang, Y. Loading of Aerogels in Self-Healable Polyurea Foam to Prepare Superhydrophobic Tough Coating with Ultra-Long Freezing Delay Time and High Durability. *Surfaces Interfaces* **2024**, *51*, No. 104763.

(30) Wang, F.; Zhuo, Y.; He, Z.; Xiao, S.; He, J.; Zhang, Z. Dynamic Anti-Icing Surfaces (DAIS). *Adv. Sci.* **2021**, *8* (21), No. 2101163.

(31) Oh, J.; Myoung, J.; Bae, J. S.; Lim, S. Etch Behavior of ALD Al2O3 on HfSiO and HfSiON Stacks in Acidic and Basic Etchants. *J. Electrochem. Soc.* **2011**, *158* (4), D217.

(32) Liu, G.; Yang, R.; Li, M. Liquid Adsorption of Basic Dye Using Silica Aerogels with Different Textural Properties. *J. Non-Cryst. Solids* **2010**, *356* (4), 250−257.
(33) Liu, Q.; Liu, Y.; Zhang, Z.; Wang, X.; Shen, J. Adsorption of Cationic Dyes from Aqueous Solution Using Hydrophilic Silica Aerogel via Ambient Pressure Drying. *Chin. J. Chem. Eng.* **2020**, *28* (9), 2467−2473.
(34) Thommes, M.; Kaneko, K.; Neimark, A. V.; Olivier, J. P.; Rodriguez-Reinoso, F.; Rouquerol, J.; Sing, K. S. W. Physisorption of Gases, with Special Reference to the Evaluation of Surface Area and Pore Size Distribution (IUPAC Technical Report). *Pure Appl. Chem.* **2015**, *87* (9−10), 1051−1069.
(35) Shen, F.-X.; Li, Y.; Chen, Z.-Y.; Cao, C.-F.; Shen, Y.-B.; Li, L.-T.; Pan, L.-Q.; Li, J.-Y.; Zhang, G.-D.; Gao, J.; Shi, Y.; Song, P.; Bae, J.; Tang, L.-C. Lightweight, Surface Hydrophobic and Flame-Retardant Polydimethylsiloxane Foam Composites Coated with Graphene Oxide via Interface Engineering. *Prog. Org. Coatings* **2024**, *189*, No. 108276.
(36) Chen, H.-Y.; Li, Y.; Wang, P.-H.; Qu, Z.-H.; Qin, Y.-Q.; Yang, L.; Li, J.-Y.; Gong, L.-X.; Zhao, L.; Zhang, G.-D.; Gao, J.-F.; Tang, L.-C. Facile Fabrication of Low-Content Surface-Assembled MXene in Silicone Rubber Foam Materials with Lightweight, Wide-Temperature Mechanical Flexibility, Improved Flame Resistance and Exceptional Smoke Suppression. *Composites, Part A* **2024**, *177*, No. 107907.
(37) Mao, M.; Yu, K.-X.; Cao, C.-F.; Gong, L.-X.; Zhang, G.-D.; Zhao, L.; Song, P.; Gao, J.-F.; Tang, L.-C. Facile and Green Fabrication of Flame-Retardant Ti3C2Tx MXene Networks for Ultrafast, Reusable and Weather-Resistant Fire Warning. *Chem. Eng. J.* **2022**, *427*, No. 131615.
(38) Qu, Y.-X.; Guo, K.-Y.; Pan, H.-T.; Wu, Z.-H.; Guo, B.-F.; Feng, X.-L.; Kong, T.-T.; Zhang, C.; Zhang, G.-D.; Zhao, L.; Gong, L.-X.; Gao, J.-F.; Liu, H.-L.; Mao, Z.-N.; Tang, L.-C. Facile Synthesis of Mechanically Flexible and Super-Hydrophobic Silicone Aerogels with Tunable Pore Structure for Efficient Oil-Water Separation. *Mater. Today Chem.* **2022**, *26*, No. 101068.
(39) Guo, B.-F.; Wang, Y.-J.; Qu, Z.-H.; Yang, F.; Qin, Y.-Q.; Li, Y.; Zhang, G.-D.; Gao, J.-F.; Shi, Y.; Song, P.; Tang, L.-C. Hydrosilylation Adducts to Produce Wide-Temperature Flexible Polysiloxane Aerogel under Ambient Temperature and Pressure Drying. *Small* **2024**, *20* (14), No. 2309272.
(40) Wu, Z.-H.; Feng, X.-L.; Qu, Y.-X.; Gong, L.-X.; Cao, K.; Zhang, G.-D.; Shi, Y.; Gao, J.-F.; Song, P.; Tang, L.-C. Silane Modified MXene/Polybenzazole Nanocomposite Aerogels with Exceptional Surface Hydrophobicity, Flame Retardance and Thermal Insulation. *Compos. Commun.* **2023**, *37*, No. 101402.
(41) Huang, Y.; Gancheva, T.; Favis, B. D.; Abidli, A.; Wang, J.; Park, C. B. Hydrophobic Porous Polypropylene with Hierarchical Structures for Ultrafast and Highly Selective Oil/Water Separation. *ACS Appl. Mater. Interfaces* **2021**, *13* (14), 16859−16868.
(42) Huang, C.; Qian, X.; Yang, R. Thermal Conductivity of Polymers and Polymer Nanocomposites. *Mater. Sci. Eng., R* **2018**, *132*, 1−22.
(43) Schiavoni, S.; D'Alessandro, F.; Bianchi, F.; Asdrubali, F. Insulation Materials for the Building Sector: A Review and Comparative Analysis. *Renewable Sustainable Energy Rev.* **2016**, *62*, 988−1011.
(44) Ozbay, S.; Erbil, H. Y. Ice Accretion by Spraying Supercooled Droplets Is Not Dependent on Wettability and Surface Free Energy of Substrates. *Colloids Surf., A* **2016**, *504*, 210−218.
(45) Nosonovsky, M.; Hejazi, V. Why Superhydrophobic Surfaces Are Not Always Icephobic. *ACS Nano* **2012**, *6* (10), 8488−8491.
(46) Chen, J.; Liu, J.; He, M.; Li, K.; Cui, D.; Zhang, Q.; Zeng, X.; Zhang, Y.; Wang, J.; Song, Y. Superhydrophobic Surfaces Cannot Reduce Ice Adhesion. *Appl. Phys. Lett.* **2012**, *101* (11), No. 111603.
(47) Kietzig, A.-M.; Hatzikiriakos, S. G.; Englezos, P. Ice Friction: The Effect of Thermal Conductivity. *J. Glaciol.* **2010**, *56* (197), 473−479.
(48) Bäurle, L.; Kaempfer, T. U.; Szabó, D.; Spencer, N. D. Sliding Friction of Polyethylene on Snow and Ice: Contact Area and Modeling. *Cold Reg. Sci. Technol.* **2007**, *47* (3), 276−289.
(49) Chen, T.; Dong, X.; Han, L.; Cong, Q.; Qi, Y.; Jin, J.; Liu, C.; Wang, M. Changing the Freezing Interface Characteristics to Reduce the Ice Adhesion Strength. *Appl. Therm. Eng.* **2023**, *230*, No. 120796.
(50) Suzuki, Y.; Duran, H.; Steinhart, M.; Kappl, M.; Butt, H.-J.; Floudas, G. Homogeneous Nucleation of Predominantly Cubic Ice Confined in Nanoporous Alumina. *Nano Lett.* **2015**, *15* (3), 1987−1992.

https://doi.org/10.1021/acsomega.4c04802
ACS Omega 2024, 9, 35864−35872